Coupling to substrate adhesions drives the maturation of muscle stress fibers into myofibrils within cardiomyocytes

Nilay Taneja†, Abigail C. Neininger†, and Dylan T. Burnette*
Department of Cell and Developmental Biology, Vanderbilt University, Nashville, TN 37232

ABSTRACT **Forces generated by heart muscle contraction must be balanced by adhesion to the extracellular matrix (ECM) and to other cells for proper heart function. Decades of data have suggested that cell–ECM adhesions are important for sarcomere assembly. However, the relationship between cell–ECM adhesions and sarcomeres assembling de novo remains untested. Sarcomeres arise from muscle stress fibers (MSFs) that are translocating on the top (dorsal) surface of cultured cardiomyocytes. Using an array of tools to modulate cell–ECM adhesion, we established a strong positive correlation between the extent of cell–ECM adhesion and sarcomere assembly. On the other hand, we found a strong negative correlation between the extent of cell–ECM adhesion and the rate of MSF translocation, a phenomenon also observed in nonmuscle cells. We further find a conserved network architecture that also exists in nonmuscle cells. Taken together, our results show that cell–ECM adhesions mediate coupling between the substrate and MSFs, allowing their maturation into sarcomere-containing myofibrils.**

Monitoring Editor
Manuel Théry
CEA, Hôpital Saint-Louis

Received: Nov 20, 2019
Revised: Apr 1, 2020
Accepted: Apr 3, 2020

INTRODUCTION

The heart generates contractile force through the shortening of sarcomeres, which consist of myosin "thick" filaments forming sliding interactions with actin "thin" filaments. Actin filaments of adjacent sarcomeres are cross-linked by α-actinin-2 at Z-discs, which are important sites for intracellular signaling and mechanical stability of cardiomyocytes (Knoll *et al.*, 2011; Kovacic-Milivojevic *et al.*, 2001). The basic functional unit of contraction within a cardiomyocyte is the myofibril, comprised of a series of sarcomeres. In healthy cardiomyocytes, contractile forces generated by myofibrils are balanced by adhesive forces, specifically at cell-extracellular matrix (ECM) contacts (referred to as costameres), which transfer these forces to the ECM, and at cell–cell contacts (referred to as intercalated discs) (Samarel, 2005; Liu *et al.*, 2016). Loss of this force balance can lead to detrimental phenotypes and disease states (Samarel, 2005; Dabiri *et al.*, 2012). Previous work has shown that cell–ECM contacts comprise the majority of sites of force generation during early cardiomyocyte spreading during the time window of myofibril assembly (McCain *et al.*, 2012). These sites of force generation are subsequently transferred to cell–cell contacts as cells start to form intercalated discs.

Early studies of cultured primary chick cardiomyocytes localized adhesion proteins, such as vinculin, to the ends of myofibrils and proposed that "adhesion plaques" serve as sites of myofibril assembly (Lu *et al.*, 1992). This idea was supported by multiple genetic studies performed in the skeletal muscle of worms and fruit flies (Volk *et al.*, 1990; Hresko *et al.*, 1994; Bloor and Brown, 1998). Knockout of proteins involved in cell–ECM adhesion, such as integrin or perlecan, resulted in fewer myofibrils compared with the knockout of myofibril components themselves. Thus, the genetic evidence suggests that cell–ECM adhesion is upstream of myofibril assembly (Sparrow and Schock, 2009). It has additionally been shown that inhibiting contraction of cultured rat primary cardiomyocytes results in a loss of adhesions (Simpson *et al.*, 1993; Sharp *et al.*, 1997). Conversely, modulating the size of adhesions by varying substrate stiffness can modulate the contractile properties of

This article was published online ahead of print in MBoC in Press (http://www.molbiolcell.org/cgi/doi/10.1091/mbc.E19-11-0652) on April 8, 2020.

†These authors contributed equally to the work.

*Address correspondence to: Dylan T. Burnette (dylan.burnette@vanderbilt.edu).

Abbreviations used: BSA, bovine serum albumin; DSF, dorsal stress fiber; ECM, extracellular matrix; FAK, focal adhesion kinase; hiCM, human induced pluripotent stem cell-derived cardiomyocyte; MSF, muscle stress fiber; PBS, phosphate-buffered saline; PEG, polyoxyethylene glycol; PFA, paraformaldehyde; SIM, structured illumination microscopy; TBST, Tris-buffered saline Tween-20.

cardiomyocytes (Jacot *et al.*, 2008; Hersch *et al.*, 2013). This indicates that there is feedback between cardiomyocyte adhesion and contractile function. Despite this evidence, the mechanistic relationship between cell–ECM adhesion and myofibril assembly has remained unclear. This has been in part due to multiple conflicting models of myofibril assembly itself (Sanger *et al.*, 2005).

Of the multiple competing models of myofibril assembly that have been proposed, the Template (aka, pre-myofibril) model has the most experimental support. First proposed by Howard Holtzer in 1984, the Template model postulated that nonmuscle stress fiber-like structures are the precursors of myofibrils (Dlugosz *et al.*, 1984). We have recently shortened Holtzer's initialism to MSFs (muscle stress fibers) for brevity (Fenix *et al.*, 2018). While there was substantial evidence from fixed cultured myocytes and tissue to support the Template/pre-myofibril model, there was little dynamic data directly demonstrating the transition of MSFs to myofibrils (Dlugosz *et al.*, 1984; Rhee *et al.*, 1994). We have recently utilized human iPSC-derived cardiomyocytes (hiCMs) to capture this transition (Fenix *et al.*, 2018). hiCMs are transcriptionally similar to embryonic and neonatal cardiomyocytes, a time at which sarcomere assembly is occurring in vivo. We reported that freshly plated hiCMs did not have sarcomeres and subsequently assembled them over 4–16 h after plating (Fenix *et al.*, 2018). Live-cell imaging of either actin or α-actinin-2 revealed that MSFs move away from the edge and obtain sarcomeres over time.

Studies in primary skeletal myocytes from β1 integrin-deficient mice proposed that cell–ECM adhesion could regulate the transition of MSFs to myofibrils, rather than the formation of MSFs themselves (Schwander *et al.*, 2003). In fixed cells, the authors observed that inactivation of β1 integrin led to a lack of myofibrils, but not MSFs (Schwander *et al.*, 2003). A more recent study, however, claimed a new model of sarcomere assembly, where cell–ECM adhesion sites serve as the site for centripetal nucleation of sarcomeres (Chopra *et al.*, 2018). In this model, a sarcomere-containing myofibril directly grows out of an adhesion, without the need for a template (i.e., MSFs). The authors imaged α-actinin-2, which marks both focal adhesions and the Z-lines of myofibrils. Indeed, a cursory glance at the movies presented gives the impression that the Z-lines are streaming out of adhesions. However, closer frame-by-frame inspection of the data revealed that these events were preformed myofibrils coming from the dorsal surface of the cell to the ventral (in focus) surface. We have now experimentally demonstrated this phenomenon (Fenix *et al.*, 2018). It is important to note that we were only able to capture these events after 24 h postplating, which is the time window in which Chopra *et al.* (2018) imaged their hiCMs.

Here, we sought to investigate the role of cell–ECM adhesion in myofibril assembly within the context of the Template/pre-myofibril model. By combining high-resolution three-dimensional imaging and multiple perturbations to focal adhesion assembly, we show that 1) dorsal stress fiber (DSF)-like actin-based structures couple myofibrils to focal adhesions, 2) focal adhesions do not serve as the direct site for nucleation of myofibrils or MSFs, and 3) stronger coupling to the ECM correlates with the ability of MSFs to mature into myofibrils.

RESULTS

The spatiotemporal relationship between cell–ECM adhesion and myofibril maturation

We first wanted to explore how adhesions, which are present on the ventral surface of the cell, are connected to myofibrils on the dorsal surface of the cell. We noticed that the relative organization of the focal adhesions and contractile structures (i.e., MSFs and myofibrils) bore a striking resemblance to that of mesenchymal crawling nonmuscle cells (Figure 1A). Indeed, we have previously noted that MSFs were similar in their organization to stress fibers found on the dorsal surface of mesenchymal cells called actin arcs (Fenix *et al.*, 2018). In mesenchymal cells, actin arcs are connected to focal adhesions through specialized actin filament-based structures called DSFs (Hotulainen and Lappalainen, 2006). To test if DSF-like structures exist in hiCMs, we examined the actin filament channel throughout the axial (Z) dimension (Figure 1, B and C; Supplemental Figure S1A). We found that diffraction-limited imaging was not able to resolve the relative axial positions of different actin filament structures, especially those close to the edges of hiCMs (Supplemental Figure S2). For this reason, we imaged actin filaments with structured illumination microscopy (SIM), which provides a ~2× increase in axial resolution. SIM revealed that strands of actin filaments extended from the ventral surface of the cell up to the dorsal surface (Figure 1B). These strands ended in the MSFs and myofibrils on the dorsal surface (Figure 1C; Supplemental Figure S1B; Supplemental Movie S1).

We next wanted to experimentally test if DSFs were mechanically coupled to MSFs and myofibrils. We hypothesized that the contractile MSFs and myofibrils could be pulling on DSFs. Therefore, we predicted that cutting DSFs would result in MSFs/myofibrils moving away from the edge of the cell. To test this possibility, we cut a DSF that appeared connected to either an MSF (Figure 1D) or a myofibril (Figure 1E) using a high intensity-focused laser. We found that cutting of the DSF resulted in translocation of the MSF or myofibril away from the edge (Figure 1, D and E). To further test mechanical coupling, we also cut a myofibril that was attached to two DSFs; one on either end (Supplemental Movie S2). On cutting, the two halves of the myofibril retracted away from each other along with the DSF each half was attached to (Supplemental Movie S2). Taken together, the localization and laser dissection experiments suggest that DSFs mechanically connect MSFs and myofibrils to adhesions.

Given the physical connection between focal adhesions and myofibrils, we next investigated if there was a temporal relationship between the relative assembly of the two structures. We imaged actin filaments and paxillin in live hiCMs during the transition of MSFs into the first myofibrils. We use the term "myofibril maturation" to describe this transition. This should not be confused with "cardiomyocyte maturation," which involves transcriptional and metabolic changes over developmental time scales (Jiang *et al.*, 2018). As previously demonstrated, MSFs translocate away from the edge and obtain sarcomeres over time (Fenix *et al.*, 2018). The purple arrowheads in Figure 2A denote this phenomenon. The paxillin channel revealed that focal adhesions also elongate during this same time period (Figure 2A, green arrowheads). Consistent with how DSFs form in mesenchymal cells (Hotulainen and Lappalainen, 2006), we observed the appearance of DSF-like connections between the elongating adhesions and maturing myofibrils (Figure 2A, yellow arrowheads). We next wanted to quantify the potential relationship between adhesion growth and myofibril maturation over time.

As focal adhesions mature, their area increases (Geiger *et al.*, 2009). Similarly, when myofibrils mature, the length of their Z-lines increases (Dabiri *et al.*, 1997). Therefore, we used total area of focal adhesions as a proxy for adhesion maturity and Z-line length as a proxy for myofibril maturity. To identify focal adhesions, we localized the adhesion protein, paxillin (Figure 2B). To identify Z-lines, we localized α-actinin-2 (Figure 2B). We then used a computer-assisted analysis method we developed to measure Z-line length

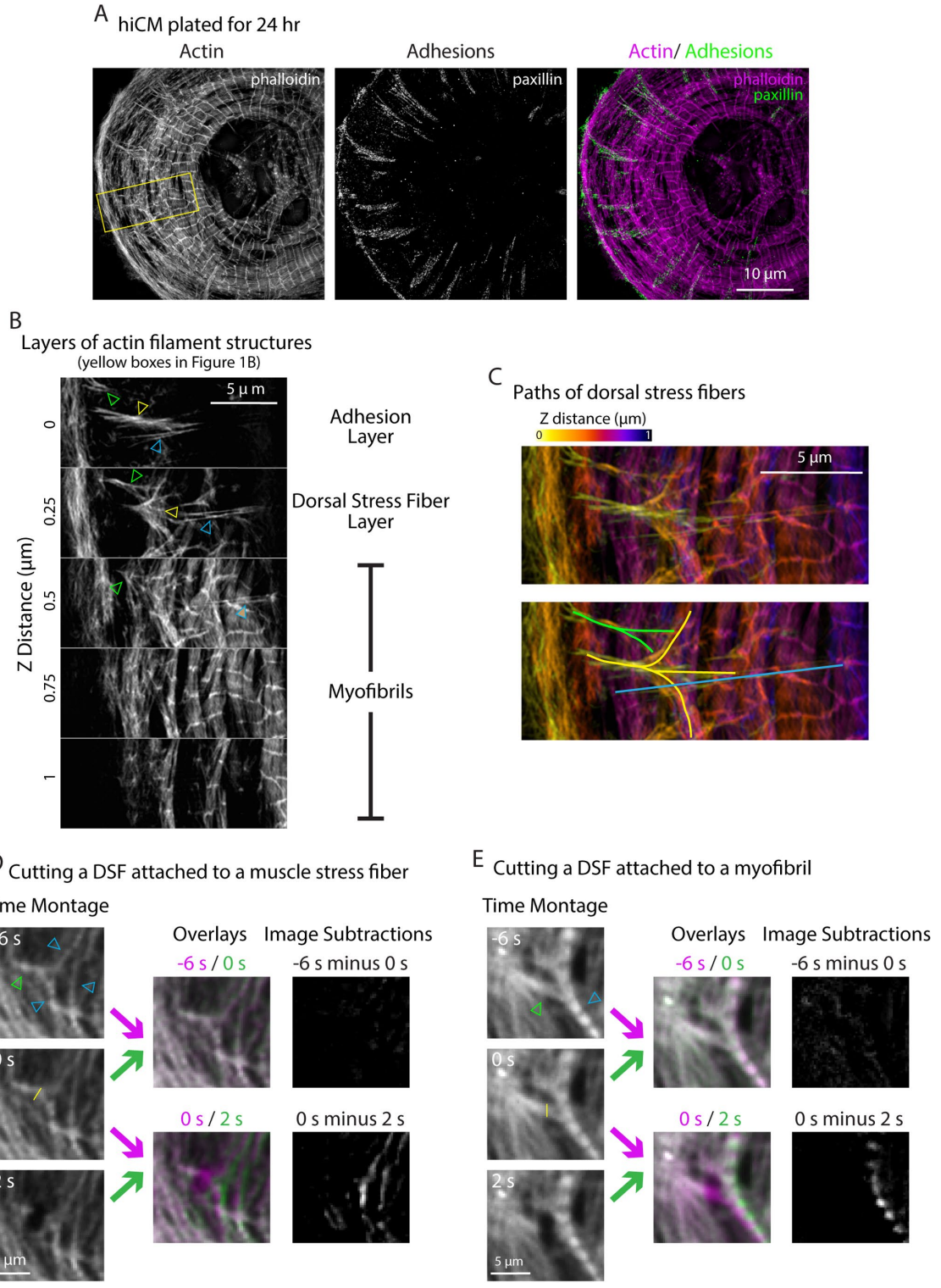

FIGURE 1: Three-dimensional organization of myofibrils and DSFs. (A) SIM of actin filaments (magenta) and paxillin (green) in hiCM plated for 24 h. (B) SIM showing the layers of actin filaments in the axial (Z) dimension from the box in A. Arrowheads denote different DSFs. (C) Three-dimensional color projection of the data in (B). Lines denote the different DSFs denoted in B. (D, E) Focused laser-mediated cutting of DSF attached to an MSF (D) or a myofibril (E) in hiCM expressing Lifeact-mApple at 16 h postplating. Green arrowheads denote DSFs and blue arrowheads denote MSF or myofibril. Yellow line denotes cut site. Temporal color-coded overlays and image subtractions show the change in positioning of the MSF or myofibril following cutting of the DSF. See Supplemental Figure S1C for uncropped views of cells.

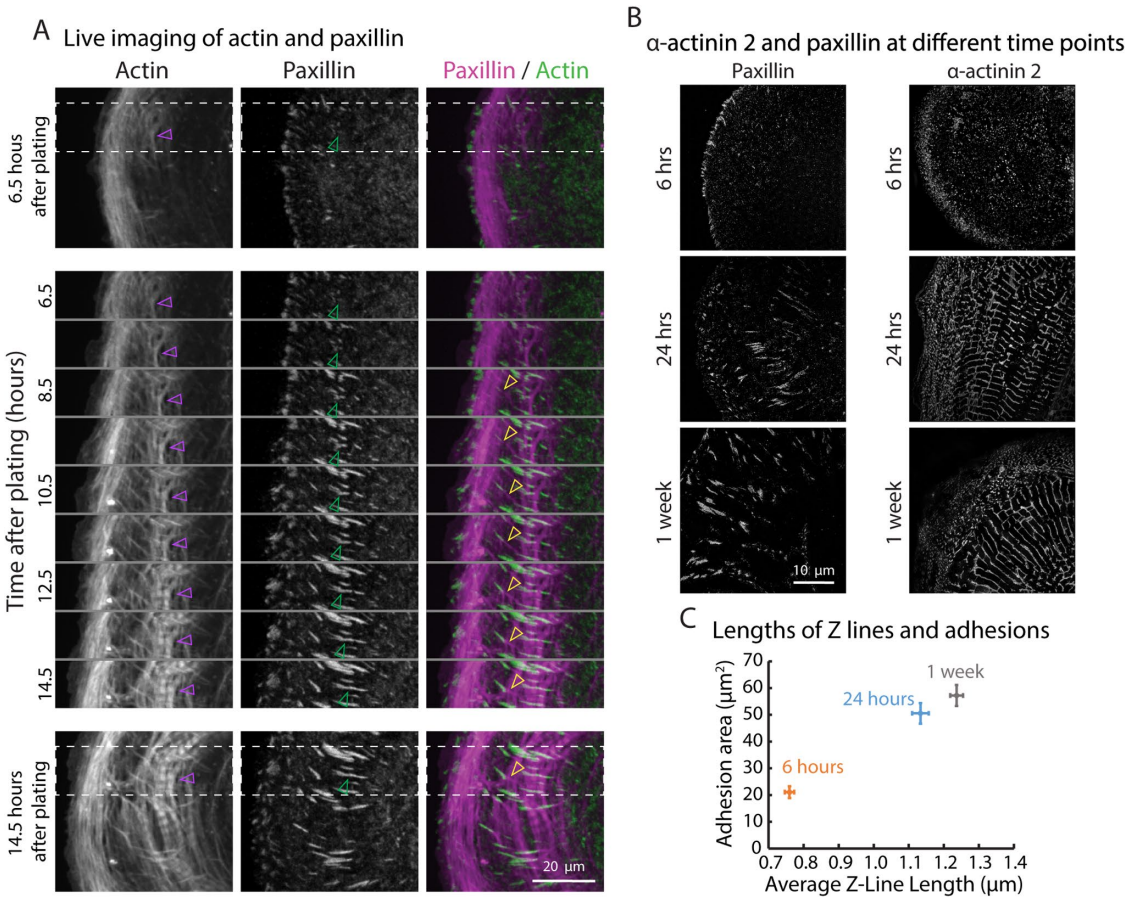

FIGURE 2: Dynamics of adhesions and myofibril maturation. (A) Time montage of actin labeled with Lifeact-mEmerald and paxillin-mCherry during myofibril assembly. The first frame (top) and last frame (bottom) are separated by a time montage of the regions shown in the boxes (dotted lines). The purple arrowhead denotes an MSF becoming a myofibril. The green arrowhead denotes a growing adhesion. The yellow arrowhead denotes an extending DSF. (B) Representative SIM images of endogenous paxillin and α-actinin-2 in hiCMs plated from 6 h, 24 h, or 1 wk. (C) Quantification of Z-line lengths and adhesion area in hiCMs plated for 6 h, 24 h, and 1 wk. Z-line measurements: 6H: $n = 58$ cells, $N = 4$ independent experiments; 24H: $n = 75$ cells, $N = 4$ independent experiments; 1 Week: $n = 81$ cells, 3 independent experiments. Adhesion measurements: 6H; $n = 38$ cells, $N = 5$ independent experiments; 24H: $n = 48$ cells, $N = 5$ independent experiments; 1 Week: $n = 28$ cells, $N = 3$ independent experiments.

and adhesion area in hundreds of cells during hiCM spreading (Supplemental Figure S3, supplemental software). We analyzed cells that were allowed to spread for 6 h, 24 h, and 1 wk postplating (Figure 2B). We chose these time points based on our previous observations on the timing of myofibril maturation. At 6 h postplating, most hiCMs were characterized by immature myofibrils with punctate Z-lines (i.e., Z-bodies). By 24 h, hiCMs contained myofibrils with elongated Z-lines. As suggested by our live data, we observed a strong positive correlation between the extent of adhesion and myofibril maturity at 6 h, 24 h, and up to 1 wk postplating (Figure 2C). We next wanted to further establish the relationship between cell–ECM adhesion and myofibril maturation by altering components of the adhesion machinery and measuring the effects on myofibril maturation.

Decreasing cell–ECM adhesion results in attenuation of myofibril maturation

We chose to start with vinculin, a component of focal adhesions that links the adhesion to the actin cytoskeleton (Carisey and Ballestrem, 2011). It was predicted two decades ago by Howard Holtzer and colleagues that vinculin would play a role during myofibril assembly (Lu *et al.*, 1992). Furthermore, knockout of vinculin in hiCMs has been shown to alter the organization of Z-lines (Chopra *et al.*, 2018). We depleted vinculin using a pooled siRNA approach and found a significant reduction in paxillin-positive area (Figure 3, A–C). To test if reduction in vinculin altered myofibril maturation, we measured the length of Z-lines after 24 h of spreading, since this is the time point at which most control cells contained myofibrils (Fenix *et al.*, 2018). Knockdown of vinculin resulted in a significant reduction in Z-line length (Figure 3, D and E). This reduction in Z-line length was in agreement with previously published data (Chopra *et al.*, 2018). We next wanted an additional measure of myofibril maturation. The incorporation of the large Z-disk protein titin is considered a marker for maturation of myofibrils (Sanger *et al.*, 2005). We localized the N-terminal region of titin, which should localize on either side of Z-lines (Figure 3F) (Wang and Greaser, 1985). In control cells plated for 24 h, we found distinct organization of titin at a mean distance of 4.1 ± 2.3 μm from the edge (Figure 3G). Knockdown of vinculin resulted in severe disruption of overall titin organization, with the first titin structures localizing 9.5 ± 3.8 μm from the edge (Figure 3G). The

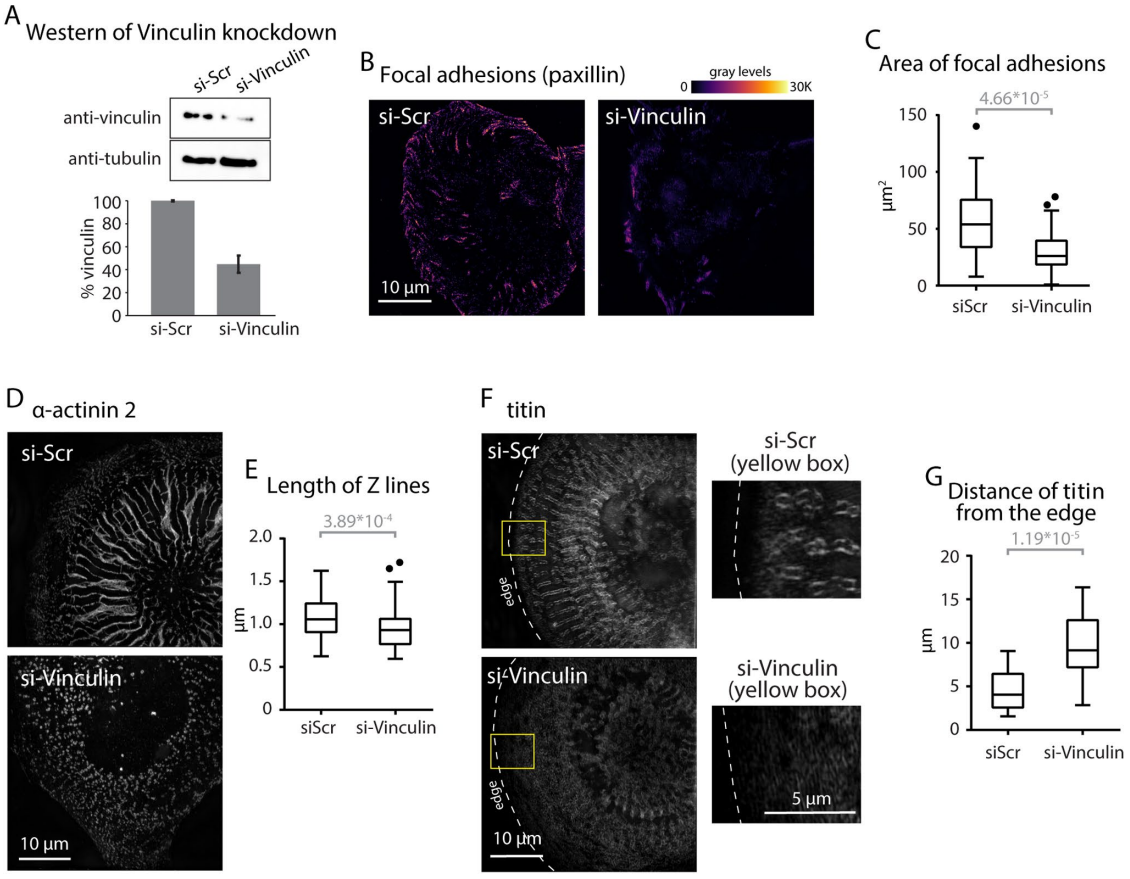

FIGURE 3: Knockdown of vinculin results in attenuation of myofibril maturation. (A) Representative Western blot for vinculin knockdown using siRNA. Tubulin was used as a loading control. Knockdown efficiency was calculated from four independent experiments. (B) Paxillin localization (single optical section) in hiCMs treated with either scrambled or vinculin siRNA. (C) Quantification of adhesion area. si-Scr: $n = 54$ cells, $N = 6$ independent experiments; si-Vinculin: $n = 30$ cells, $N = 4$ independent experiments. (D) α-Actinin-2 localization (maximum Z-projection) in hiCMs treated with either scrambled or vinculin siRNA. (E) Quantification of average length of Z-lines. si-Scr: $n = 131$ cells, $N = 6$ independent experiments; si-Vinculin: $n = 69$ cells, $N = 5$ independent experiments. (F) Localization of titin in hiCMs treated with either scrambled or vinculin siRNA. (G) Quantification of distance of titin localization from the cell edge. si-Scr: $n = 19$ cells, $N = 3$ independent experiments; si-Vinculin: $n = 21$ cells, $N = 3$ independent experiments. Exact p values are stated in the graphs.

effects of vinculin knockdown on adhesion area, Z-line length, and titin organization were recapitulated using a single siRNA mediated knockdown approach (Supplemental Figure S4, A–D).

In nonmuscle cells, vinculin is thought to act as a "clutch" that mechanically couples focal adhesions to actin stress fibers (e.g., actin arcs) to impede their rearward translocation (Thievessen *et al.*, 2013). As a result, we asked if vinculin could also be slowing the translocation of MSFs. We previously reported that MSFs translocate away from the edge and then slow down as they transition into myofibrils, which undergo little translocation (Fenix *et al.*, 2018). Therefore, we quantified the rate of rearward movement of MSFs in control versus vinculin-depleted cells. We used kymography to measure the rates of MSF translocation (Figure 4, A and B). In control cells, we found MSFs underwent rearward translocation at comparable rates as our previous report (Figure 4, A, B, and E). Vinculin knockdown resulted in a significant increase in MSF translocation rates (Figure 4, C and E). This is consistent with a potential role for cell–ECM adhesion in slowing the translocation of MSFs. We next wanted to test if reduction of adhesion size through altering other adhesion components could also attenuate myofibril maturation.

Talin is a focal adhesion protein that directly binds β integrins through its N-terminal "head" domain and to vinculin through its C-terminal "tail" domain (Dumbauld *et al.*, 2013). As a result, talin binding to vinculin leads to focal adhesion strengthening by linking vinculin to integrins (Case *et al.*, 2015). It has been previously reported that overexpression of the head domain of talin acts in a dominant negative manner, resulting in attenuation of focal adhesion signaling (Tan *et al.*, 2015). We hypothesized that expression of talin head domain should result in reduction in focal adhesion area, similar to vinculin knockdown. Therefore, we measured paxillin-positive area in hiCMs expressing talin head-mEGFP (Figure 5, A and C). We found a marked decrease in focal adhesion area in hiCMs expressing talin head-mEGFP versus control cells (Figure 5, B and C; Supplemental Figure S5). We also found that this decrease in adhesion area correlated with a decrease in Z-line length, as well as an increase in the distance from the edge at which titin localizes (Figure 5, D–G). The rate of MSF translocation also increased in hiCMs expressing talin head-mEGFP (Figure 5H).

We next investigated the role of focal adhesion kinase (FAK), which is a key scaffolding and signaling protein at focal adhesions

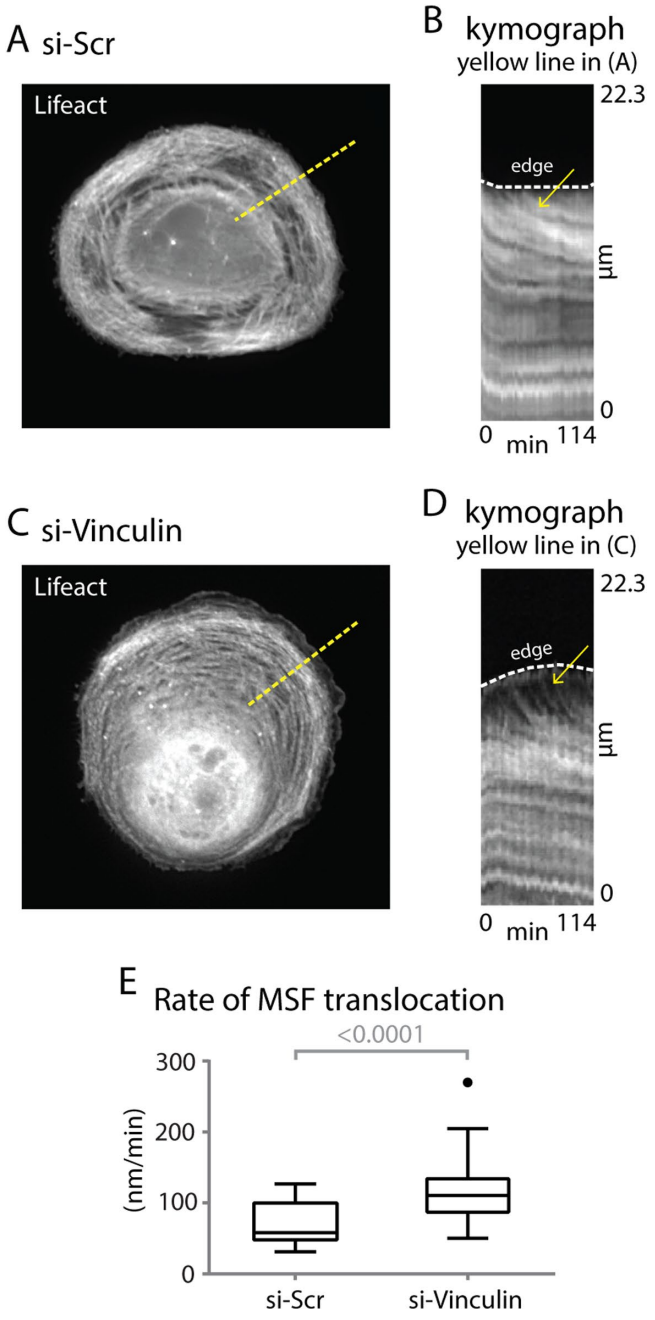

FIGURE 4: Knockdown of vinculin results in faster translocation of MSFs. (A) Control (scrambled siRNA-treated) cell expressing Lifeact-mApple 16 h postplating. (B) Kymograph generated using yellow line in A. Yellow arrow denotes MSFs translocating away from the edge (dotted white line). (C) Vinculin-depleted cell expressing Lifeact-mApple 16 h postplating. (D) Kymograph generated using yellow line in C. Yellow arrow denotes MSFs translocating away from the edge (dotted white line). (E) Quantification of MSF translocation rates in control vs. vinculin-depleted cells. si-Scr: $n = 30$ MSFs from 19 cells; si-Vinculin: $n = 22$ MSFs from 14 cells; $N = 3$ independent experiments. Exact p values are stated in the graphs.

necessary for regulating focal adhesion growth (Parsons *et al.*, 2000). A previous study has suggested that knocking down FAK in skeletal muscle precursors (i.e., myoblasts) reduced focal adhesions as well as attenuated myofibril formation (Quach and Rando, 2006). We asked whether this role for FAK is conserved in cardiomyocytes. To that end, we depleted hiCMs of FAK using a pooled siRNA approach (Figure 6A) and first measured focal adhesion area. Consistent with previous reports (Quach and Rando, 2006), we found a significant reduction in focal adhesion area on knockdown of FAK (Figure 6, B and C). In correlation with this reduction in adhesion, we found a decrease in Z-line length as well as an increase in the distance from the edge at which titin localized (Figure 6, D–G). We verified these phenotypes using single siRNA-mediated knockdown of FAK (Supplemental Figure S4, E–H). Furthermore, depletion of FAK resulted in increased rates of MSF translocation (Figure 6H). Taken together, we used four different methods to reduce focal adhesions in hiCMs. Our data suggest that reducing focal adhesion area correlates with attenuation of myofibril maturation and an increase in rate of MSF translocation. We next wanted to increase adhesion area to test if it would result in increased or accelerated myofibril maturation.

Increasing ECM adhesion results in precocious myofibril maturation

It has been shown in nonmuscle cells that pharmacologically disrupting the kinase activity of FAK leads to inhibition of adhesion turnover without affecting adhesion assembly, resulting in increase in adhesion area (Slack-Davis *et al.*, 2007; Taneja *et al.*, 2016). Therefore, we used a specific small-molecule inhibitor, PF-228, to disrupt the kinase activity of FAK in hiCMs. The autophosphorylation of FAK at Y397 is classically used as a readout for FAK kinase activity (Schaller *et al.*, 1994; Slack-Davis *et al.*, 2007; O'Brien *et al.*, 2014). We found that treatment of hiCMs with PF-228 led to a nearly complete loss of localization of pFAK from adhesions (Figure 7A). Treatment of hiCMs with PF-228 led to a small increase in focal adhesion area at 24 h postplating, but this was not significant (Supplemental Figure S6). Furthermore, there was a significant, but small change in Z-line length (Supplemental Figure S6). We wondered whether any potential effects of FAK inhibition could be observed at earlier time points in plating when the first myofibrils are assembling. We previously showed that the first myofibrils arise 4–16 h after plating (Fenix *et al.*, 2018). Therefore, we chose to investigate the relationship between focal adhesions and myofibrils at 6 h postplating. Indeed, we found that at 6 h postplating, hiCMs treated with PF-228 had a significantly higher adhesion area (Figure 7, B–C). Strikingly, we found that hiCMs treated with PF-228 also had significantly longer Z-lines, as well as closer titin localization to the edge (Figure 7, D–G). Furthermore, we found that PF–228-treated hiCMs had slower rates of MSF translocation compared with control hiCMs (Figure 7H). We next wanted to test if the correlation between an increase in adhesion area and precocious myofibril assembly was specific to FAK inhibition. Therefore, we wanted to increase focal adhesion size without any genetic or pharmacological perturbations.

It has been shown in nonmuscle cells that increasing the concentration of the ECM protein, fibronectin, leads to larger focal adhesions (Gupton and Waterman-Storer, 2006; Taneja *et al.*, 2016). As our standard procedure, we plate hiCMs on glass coverslips coated with 10 µg/ml fibronectin. As such, all the previous experiments presented here were performed with this coating concentration. To test if increasing fibronectin would increase focal adhesion area in hiCMs, we plated them on glass coverslips coated with 50 µg/ml fibronectin, as we have done previously using nonmuscle cells (Taneja *et al.*, 2016). At 6 h postplating, we found that hiCMs plated on 50 µg/ml fibronectin had a higher paxillin-positive adhesion area compared with control hiCMs plated on 10 µg/ml fibronectin (Figure 8, A and B). This increase in adhesion area correlated with an increase in Z-line length as well as closer titin localization to the edge

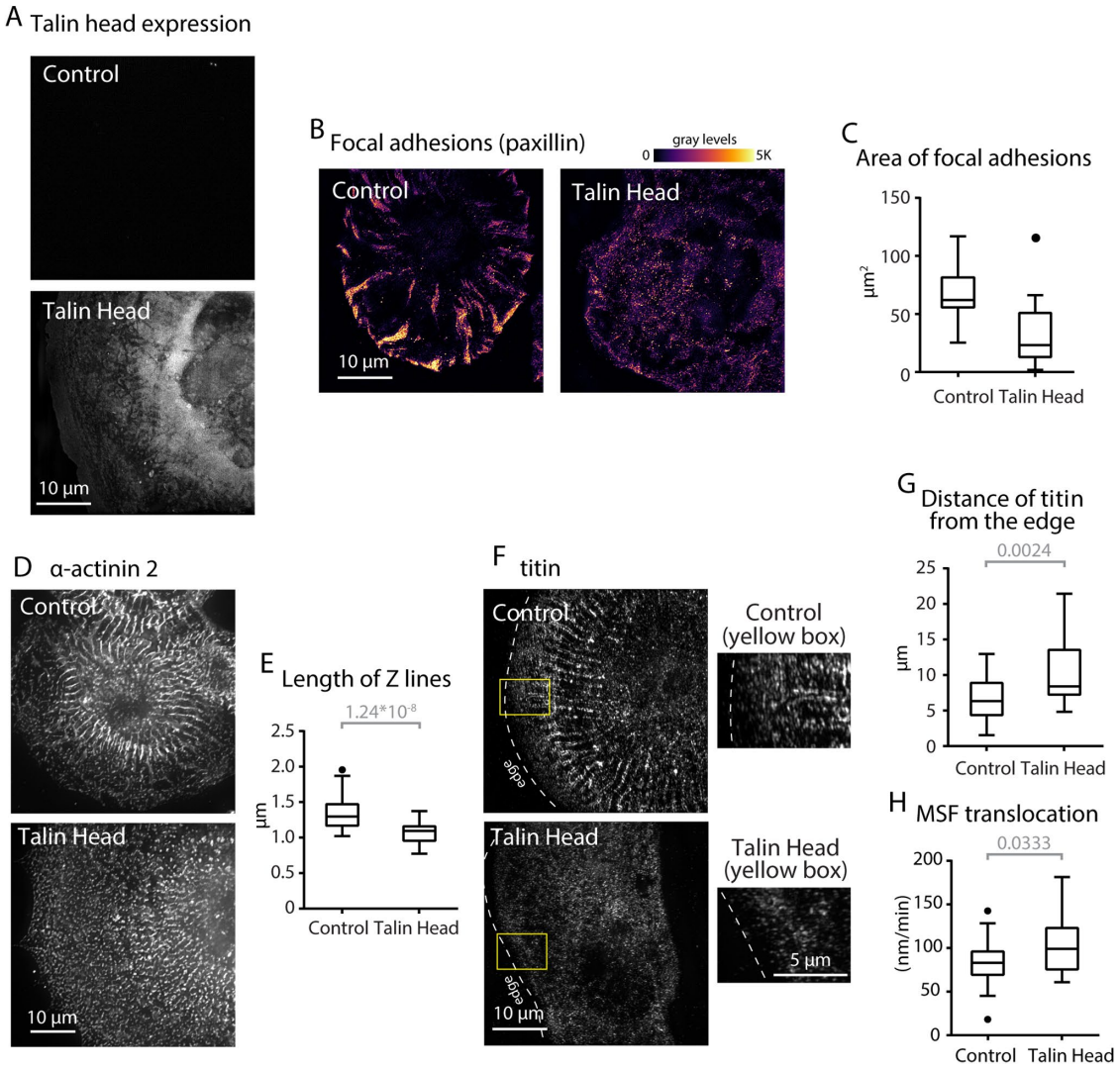

FIGURE 5: Expression of talin head domain results in attenuation of myofibril maturation. (A) Representative hiCM expressing talin head-mEGFP vs. nonexpressing hiCM. (B) Paxillin localization (single optical section) in hiCM overexpressing talin head-mEGFP vs. a nonexpressing hiCM. (C) Quantification of adhesion area. Nonexpressing: $n = 21$ cells; talin head-mEGFP: $n = 22$ cells, $N = 3$ independent experiments each. (D) α-Actinin-2 localization (maximum Z-projection) in hiCM overexpressing talin head-mEGFP vs. a nonexpressing hiCM. (E) Quantification of average Z-lines length. Nonexpressing: $n = 43$ cells; talin head-mEGFP: $n = 36$ cells; $N = 3$ independent experiments each. (F) Localization of titin in hiCM overexpressing talin head-mEGFP vs. a nonexpressing hiCM. (G) Quantification of distance of titin localization from the cell edge. Nonexpressing: $n = 19$ cells; Talin head: $n = 21$ cells, $N = 3$ independent experiments each. (H) Quantification of MSF translocation rates in control hiCMs vs. hiCMs overexpressing talin head = mEGFP. Control: $n = 25$ MSFs from 16 cells; talin head-mEGFP: $n = 26$ MSFs from 17 cells; $N = 3$ independent experiments. Exact p values are stated in the graphs.

(Figure 8, C–F). The rate of MSF translocation was also significantly slower compared with control hiCMs plated on 10 µg/ml fibronectin (Figure 8G). Of note, focal adhesion area and Z-line length were not significantly different for hiCMs plated on 10 or 50 µg/ml fibronectin at 24 h postplating, similar to what we observed with FAK inhibition (Supplemental Figure S6). Taken together, our data suggest that increasing focal adhesion area correlated with precocious myofibril maturation.

DIAPH1 is required for the maturation of myofibrils

We next wanted to further investigate the mechanism controlling substrate coupling during myofibril maturation. As DSFs form the connection between adhesions and myofibrils, we hypothesized that reducing this connection could lead to less mature myofibrils. In nonmuscle cells, the actin filament nucleator DIAPH1 is known to be critical for focal adhesion growth and its depletion results in fewer and smaller focal adhesions (Riveline *et al.*, 2001; Fessenden *et al.*, 2018). We previously showed that DIAPH1 is expressed in hiCMs using RNAseq (Fenix *et al.*, 2018). In that study, we also showed that another formin, FHOD3, is critical for the assembly of myofibrils (Fenix *et al.*, 2018). However, FHOD3 only localized to MSFs and myofibrils but not to DSFs (Fenix *et al.*, 2018). To examine whether DIAPH1 localized to DSFs, we expressed DIAPH1-mEGFP. In contrast to FHOD3, we found that DIAPH1 localized to the actin filaments of DSFs (Figure 9A). Furthermore, depletion of DIAPH1 using siRNA resulted in a reduction of DSFs but not MSFs (Figure 9, B and C).

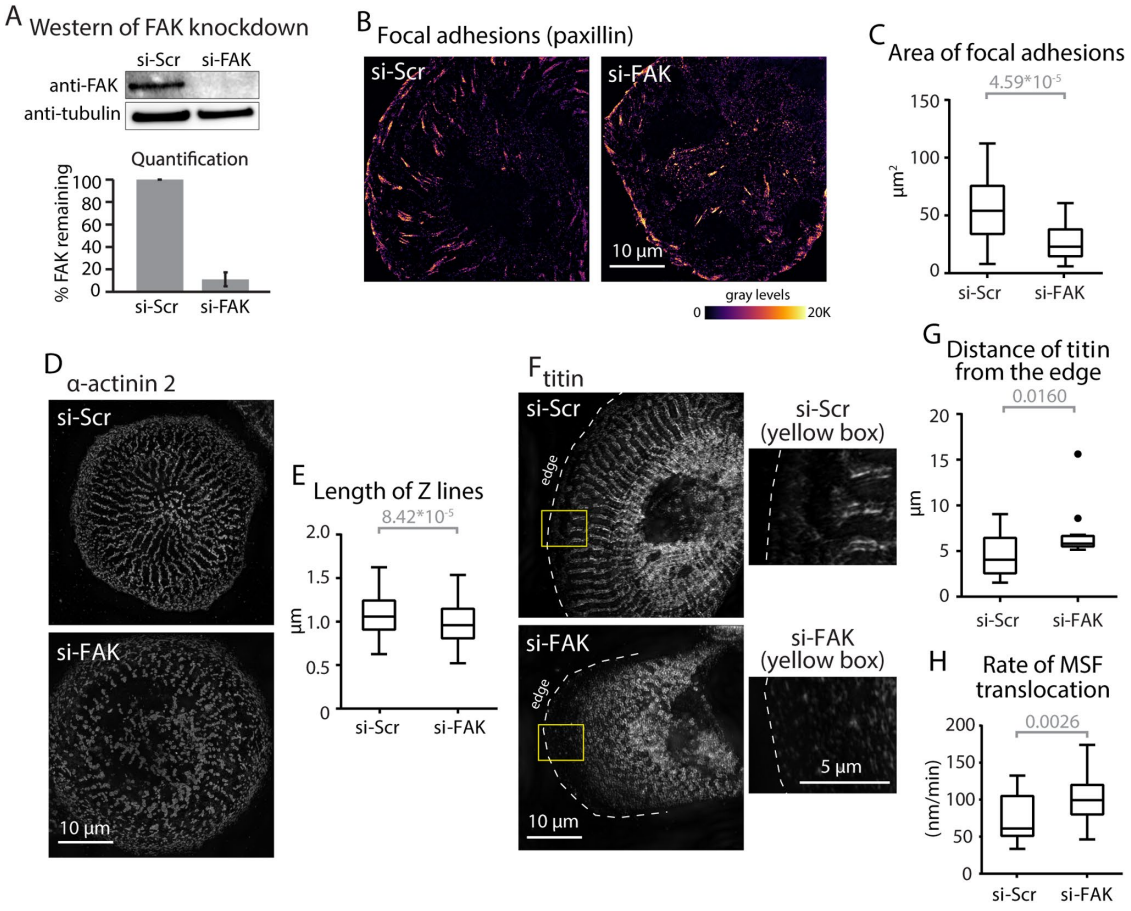

FIGURE 6: Knockdown of FAK results in attenuation of myofibril maturation. (A) Representative Western blot for FAK knockdown using siRNA. Tubulin was used as a loading control. Knockdown efficiency was calculated from three independent experiments. (B) Paxillin localization (single optical section) in hiCMs treated with either scrambled or FAK siRNA. (C) Quantification of adhesion area in FAK-depleted cells. si-FAK: $n = 36$ cells, $N = 4$ independent experiments. The si-Scr dataset is the same as in Figure 3C. (D) α-Actinin-2 localization (maximum Z-projection) in hiCMs treated with either scrambled or FAK siRNA. (E) Quantification of average length of Z-lines in FAK-depleted cells. si-FAK: $n = 106$ cells, $N = 4$ independent experiments. The si-Scr dataset is the same as in Figure 3E. (F) Localization of titin in hiCMs treated with either scrambled or FAK siRNA. (G) Quantification of distance of titin localization from the cell edge. si-FAK: $n = 12$ cells, $N = 3$ independent experiments. The si-Scr dataset is the same as in Figure 3F. (H) Quantification of MSF translocation rates in FAK-depleted cells vs. scrambled siRNA-treated hiCMs. si-FAK: $n = 25$ MSFs from 16 cells; $N = 3$ independent experiments. The si-Scr dataset is the same as in Figure 4E. Exact p values are stated in the graphs.

We next examined if DIAPH1 knockdown reduced focal adhesions and myofibril maturation. Indeed, we found that hiCMs did have a significant reduction in focal adhesion area after DIAPH1 depletion using pooled siRNA (Figure 9, D and E). Further establishing the correlation between focal adhesion area and myofibril maturation, we found a significant decrease in Z-line length (Figure 9, F and G). There was also an increase in the distance from the edge at which titin localized in DIAPH1-depleted cells (Figure 9, H and I). The phenotypes observed for focal adhesion area, Z-line length, and titin organization were recapitulated using single siRNA-mediated knockdown of DIAPH1. Further supporting the hypothesis that DIAPH1 is required for substrate coupling in hiCMs, we found a significant increase in the rate of MSF translocation (Figure 9J).

DISCUSSION

Here we present a new model of how cell–ECM adhesions regulate the maturation of sarcomere-containing myofibrils (Figure 10). We started by examining the architecture of focal adhesions relative to the contractile machinery in hiCMs during de novo assembly of myofibrils. Sarcomeres formed on the top (dorsal) surface of the cell (Fenix *et al.*, 2018), while adhesions matured on the bottom (ventral) surface of the cell. In striking resemblance to the architecture of actin stress fibers in nonmuscle cells, we found thin, actin-based connections spanning the axial distance between focal adhesions and myofibrils. We showed using laser-mediated cutting that DSFs mechanically link both MSFs and myofibrils to focal adhesions. Live imaging of adhesions and actin filaments during myofibrillogenesis revealed that these structures arise and elongate out of focal adhesions as MSFs translocate away from the edge and mature into myofibrils. This results in the long axis of focal adhesions being parallel to the long axis of Z-lines.

In our attempt to modulate adhesion area, our results have implicated a canonical adhesion pathway that is well characterized in nonmuscle cells. We started with the hypothesis that this canonical signaling axis would be conserved in cardiomyocytes. Previous superresolution studies have elaborated the nanoscale architecture of focal adhesions, revealing layers of focal adhesion components

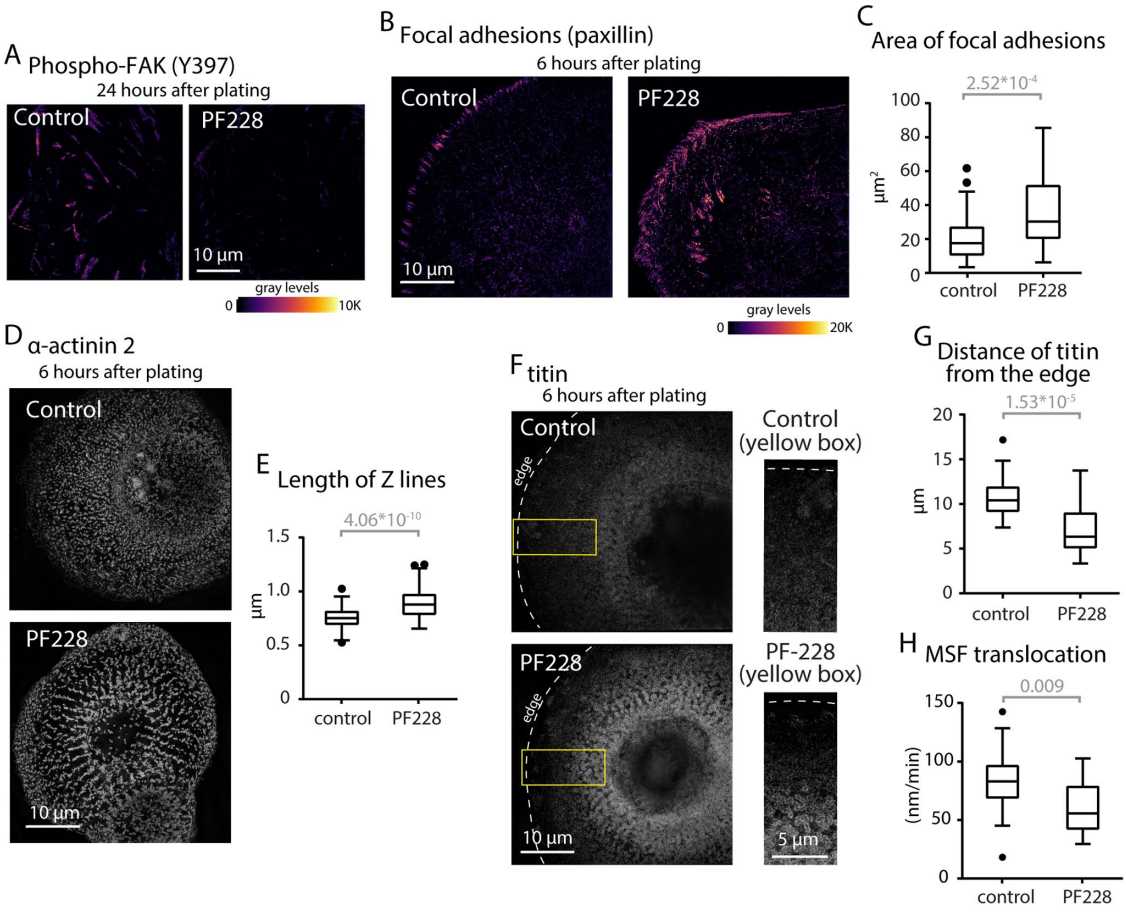

FIGURE 7: Inhibition of FAK kinase activity results in precocious myofibril maturation. (A) Localization of pFAK Y397 in control or 3 µM PF-228-treated hiCMs 24 h postplating. (B) Paxillin localization (single optical section) in control vs. PF-228-treated hiCMs 6 h postplating. (C) Quantification of adhesion area in PF-228-treated cells. Control: $n = 38$ cells, $N = 5$ independent experiments. PF-228: $n = 44$ cells, $N = 4$ independent experiments. (D) α-actinin-2 localization (maximum Z-projection) in control vs. PF-228-treated hiCMs 6 h postplating. (E) Quantification of average length of Z-lines in PF-228-treated hiCMs. Control: $n = 58$ cells, $N = 4$ independent experiments; PF-228: $n = 107$ cells, $N = 4$ independent experiments. (F) Localization of titin in control vs. PF–228-treated hiCMs after 6 h of spreading. (G) Quantification of distance of titin localization from the cell edge. Control: $n = 23$ cells; PF-228: $n = 23$ cells; $N = 3$ independent experiments each. (H) Quantification of MSF translocation rates in PF–228-treated cells vs. control. PF-228: $n = 24$ MSFs from 17 cells; $N = 3$ independent experiments. The control data set is the same is in Figure 5H. Exact p values are stated in the graphs.

(Kanchanawong *et al.*, 2010). Here we modulate each of these layers and reveal multiple positive correlations between the extent of adhesion and myofibril maturation. We modulated the integrin layer by increasing the concentration of fibronectin, the signaling layer by modulating talin and FAK, the force transduction layer by modulating vinculin, and the actin regulatory layer by modulating DIAPH1. Interestingly, these data revealed that perturbations that led to reduced adhesion area and decreased MSF maturation correlated with an increase in the rate of MSF translocation, while perturbations that led to increased adhesion resulted in a decrease in the rate of MSF translocation.

The inverse relationship between the rate of MSF translocation and the extent of adhesion parallels observations made in migrating cells. In migrating cells, adhesions slow the movement of actin arcs (Alexandrova *et al.*, 2008; Burnette *et al.*, 2011), which are the orthologs of MSFs (Fenix *et al.*, 2018). Actin arcs are physically linked to focal adhesions through DSFs (Hotulainen and Lappalainen, 2006; Burnette *et al.*, 2014). DIAPH1 has been shown to be required for DSF assembly in nonmuscle cells (Hotulainen and Lappalainen, 2006). Therefore, it was not surprising that knockdown of DIAPH1 led to an increase in the rate of MSF translocation. DSFs are linked to adhesions through vinculin, which has been proposed to act as a clutch in nonmuscle cells (Thievessen *et al.*, 2013). Indeed, MSF translocation was also accelerated on vinculin depletion. Talin mechanically links vinculin to integrins. In nonmuscle cells, overexpression of the head domain of talin disrupts the ability of endogenous talin to bind integrins, thus effectively losing this mechanical coupling (Tan *et al.*, 2015). In line with the vinculin depletion phenotype, overexpression of the head domain of talin also accelerated MSF translocation.

These multiple correlations between cell–ECM adhesion and MSF translocation, as well as direct mechanical coupling through DSFs, strongly suggest a role for mechanical forces in the maturation of myofibrils. Focal adhesions are ideally suited for allowing an increase in tension since they can both sense and adapt to the magnitude and direction of mechanical forces (Janostiak *et al.*, 2014; Swaminathan *et al.*, 2017). Components such as integrins, talin, and vinculin are mechano-sensitive (Katsumi *et al.*, 2005;

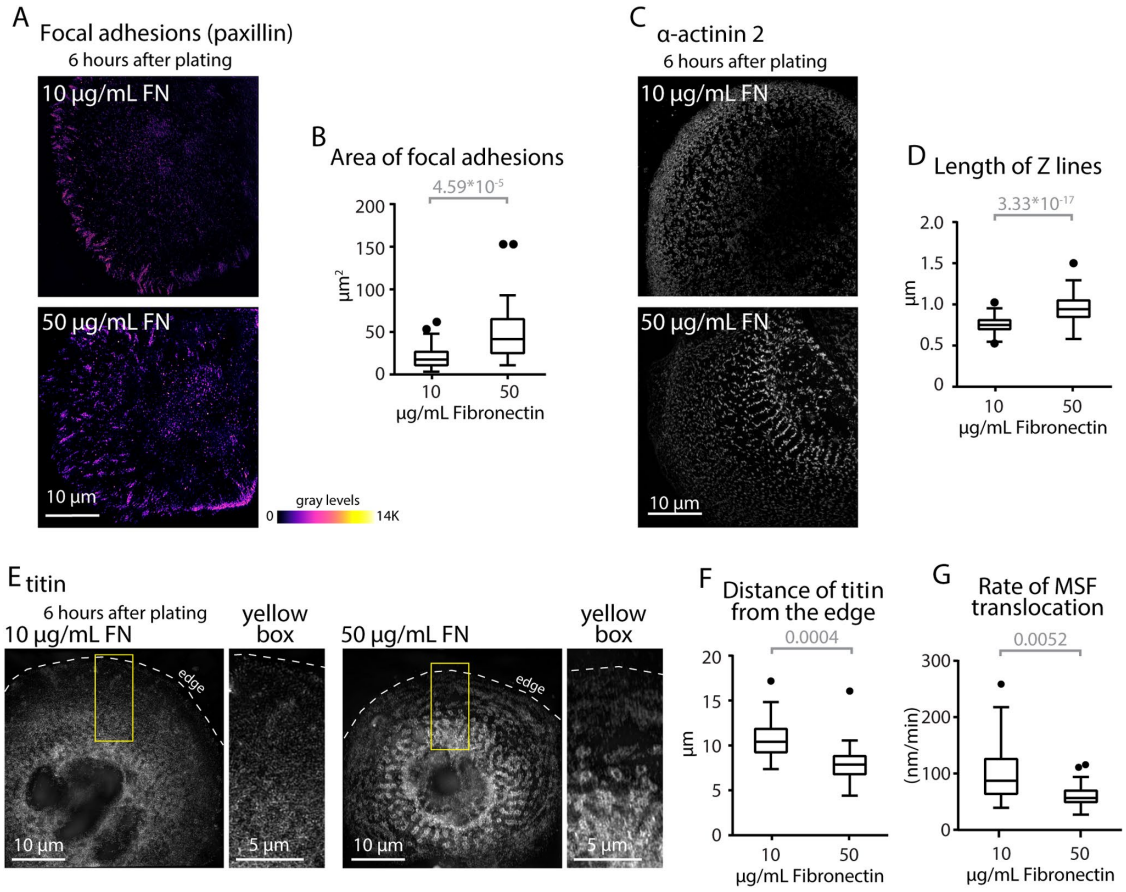

FIGURE 8: Increasing fibronectin concentration results in precocious myofibril maturation. (A) Paxillin localization (single optical section) in hiCMs plated on either 10 µg/ml or 50 µg/ml fibronectin. (B) Quantification of adhesion area in hiCMs plated on either 10 µg/ml or 50 µg/ml fibronectin; 50 µg/ml: $n = 47$ cells, $N = 5$ independent experiments. The 10 µg/ml dataset is the same as Figure 8C. (C) α-Actinin-2 localization (maximum Z-projection) in hiCMs plated on either 10 µg/ml or 50 µg/ml fibronectin. (D) Quantification of average length of Z-lines in hiCMs plated on either 10 µg/ml or 50 µg/ml fibronectin; 50 µg/ml: $n = 201$ cells, $N = 6$ independent experiments. The 10 µg/ml dataset is the same as Figure 8E. (E) Localization of titin in hiCMs plated on either 10 µg/ml or 50 µg/ml fibronectin. (F) Quantification of distance of titin localization from the cell edge; 50 µg/ml: $n = 23$ cells, $N = 3$ independent experiments. The 10 µg/ml dataset is the same as Figure 8F. (G) Quantification of MSF translocation rates in hiCMs plated on either 10 µg/ml or 50 µg/ml fibronectin; 50 µg/ml: $n = 20$ MSFs from 12 cells; $N = 3$ independent experiments. The 10 µg/ml dataset is the same as in Figure 5H. Exact p values are stated in the graphs.

del Rio *et al.*, 2009; Pasapera *et al.*, 2010); that is, they change their structural conformation on application of mechanical forces. Furthermore, it was reported that only a small proportion of talin molecules at cell–ECM attachment sites in the *Drosophila* flight muscle experience significant forces, suggesting a large pool of talin is primed for adapting to changes in load (Lemke *et al.*, 2019). Therefore, our data support a model where adhesions could serve as load-bearing sites and allow an increase in mechanical tension in MSFs, which would allow their maturation into myofibrils (Figure 10). Indeed, in the flight muscles of *Drosophila*, the establishment of cell–ECM sites with tendons precedes the maturation of stress fibers to myofibrils (Lemke and Schnorrer, 2017).

A bidirectional interplay between myofibrils and cell–ECM adhesions has also been implicated using computational modeling, where it was proposed that myofibrils and stress fibers form along the maximal principal stress direction (Yuan *et al.*, 2017). Interestingly, cell–ECM adhesion was dominant over the contribution of cell shape to determine the direction of stress; "immature" iPSC derived cardiomyocytes with uniformly arranged smaller adhesions formed radially arranged myofibrils on square micropatterns, while more mature neonatal cardiomyocytes with larger adhesions formed linear substrate attached myofibrils (Yuan *et al.*, 2017). Our data are in agreement with these theoretical predictions, since trypsinized hiCMs form radially arranged focal adhesions at early time points (6 h, Figure 2B) and thus form radially arranged myofibrils. At later time points (beyond 24 h), as adhesions grow larger, a symmetry-breaking process occurs where these myofibrils linearize and become substrate attached.

A recent study claimed to have delved into the fundamental mechanics of sarcomere assembly, where they propose that myofibrils stream out of "protocostameres" (i.e., focal adhesions) through a "centripetal" assembly mechanism (Chopra *et al.*, 2018). It is important to note again that the authors made these claims about "de novo" sarcomere assembly during a time window when sarcomeres are already assembled. The apparent appearance of myofibrils perpendicular to focal adhesions was interesting, and different than the parallel arrangement we find during sarcomere assembly. This is an effect of imaging the ventral plane of the cell and capturing the

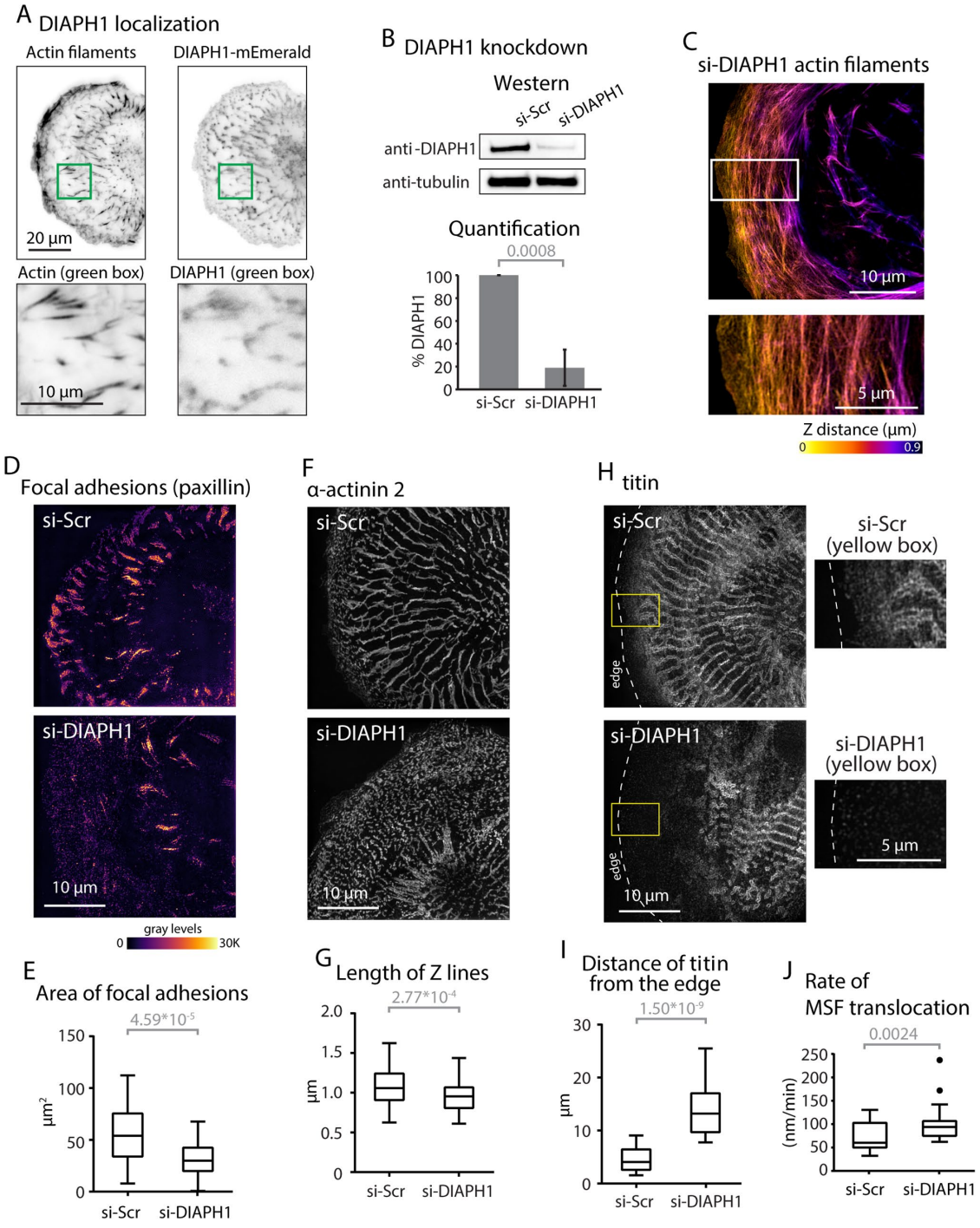

FIGURE 9: Knockdown of DIAPH1 results in attenuation of myofibril maturation. (A) Total internal reflection microscopy (TIRF) image showing the ventral section of an hiCM spread for 24 h. Actin filaments (phalloidin) and DIAPH1-mEmerald are shown in inverted gray. Note the colocalization of DIAPH1 with actin filaments associated with focal adhesions. (B) Representative Western blot for DIAPH1 knockdown using siRNA. Tubulin was used as a loading control. Knockdown efficiency was calculated from three independent experiments. (C) Three-dimensional SIM of actin filaments in a si-DIAPH1 KD hiCM at 24 h postplating. Note the lack of prominent DSFs. (D) Paxillin localization (single optical section) in hiCMs treated with either scrambled or DIAPH1 siRNA. (E) Quantification of adhesion area in DIAPH1- depleted cells. si-DIAPH1: $n = 33$ cells, $N = 4$ independent experiments. The si-Scr dataset is the same as Figure 3C. (F) α-Actinin-2 localization (maximum Z-projection) in hiCMs treated with either scrambled or DIAPH1 siRNA. (G) Quantification of average length of Z-lines in DIAPH1-depleted cells. si-DIAPH1: $n = 58$ cells, $N = 3$ independent experiments. The si-Scr dataset is the same as Figure 3E. (H) Localization of titin in hiCMs treated with either scrambled or DIAPH1 siRNA. (I) Quantification of distance of titin localization from the cell edge. si-DIAPH1: $n = 23$ cells, $N = 3$ independent experiments. The si-Scr dataset is the same as Figure 3F. (J) Quantification of MSF translocation rates in DIAPH1-depleted cells vs. scrambled siRNA-treated hiCMs. si-DIAPH1: $n = 25$ MSFs from 16 cells; $N = 3$ independent experiments. The si-Scr dataset is the same as in Figure 4E. Exact p values are stated in the graphs.

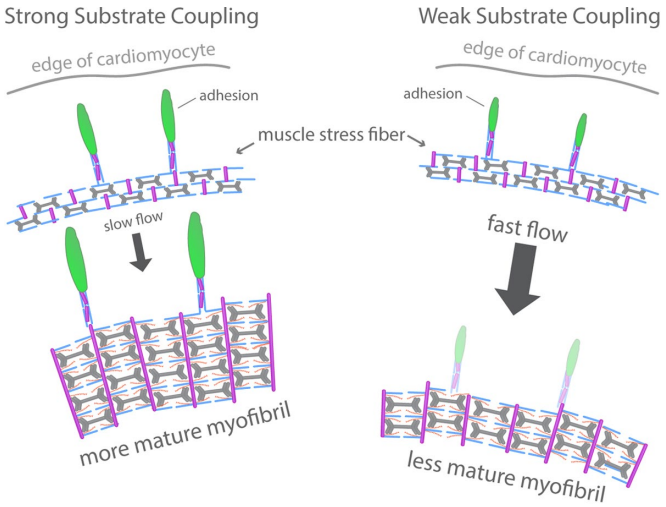

FIGURE 10: Working model for the role of substrate adhesion in myofibril maturation. Increasing cell–ECM adhesion results in greater mechanical coupling of MSFs to the ECM through DSFs. This is accompanied by slowing down of MSFs as they translocate away from the edge. Greater substrate coupling leads to the transition of the MSF to a myofibril, possibly by increased mechanical forces. Decreasing cell–ECM adhesion leads to reduced mechanical coupling, accompanied by faster translocation of MSFs and an inability to mature into force-generating myofibrils.

preformed myofibrils falling down from the dorsal surface, a phenomenon observed routinely in nonmuscle cells (Hotulainen and Lappalainen, 2006; Tojkander *et al.*, 2015). In nonmuscle cells, actin arcs on the dorsal surface fuse with at least two DSFs as they move to the ventral surface and convert to a ventral stress fiber with an adhesion at both ends (Hotulainen and Lappalainen, 2006; Tojkander *et al.*, 2015). The data from Chopra *et al.* (2018) appear to support such a mechanism of creating ventrally attached myofibrils and may be a manifestation of the symmetry breaking that occurs at later stages of hiCM spreading. We speculate DSFs are key structures that may relay the direction of principal stress from adhesions to MSFs or myofibrils.

Furthermore, Chopra *et al.* (2018) reported that knockout of β-myosin II led to a decrease in sarcomere content. This led the authors to propose that a force balance between β-myosin II, but not other myosin II paralogs, and focal adhesions directs the centripetal assembly of sarcomeres. Interestingly, subsequent studies have called into question the relative roles of the myosin II paralogs during sarcomere formation (Fenix *et al.*, 2018; Yang *et al.*, 2018). Another lab has also generated β-myosin II knockout hiCMs, and sarcomere formation in these cells still occurs (Yang *et al.*, 2018). This calls into question the requirement for β-myosin II in sarcomere formation. Furthermore, we have recently shown that knockdown of "nonmuscle" myosin IIs does lead to attenuation of sarcomere formation (Fenix *et al.*, 2018). These requirements are also mirrored in Drosophila flight muscles, where nonmuscle myosin II-mediated tension, but not muscle myosin II, was required for the increased ordering in actin filaments (Loison *et al.*, 2018).

It is important to note that our data suggest that centripetal assembly does, in part, contribute to myofibril formation. Centripetal assembly is likely to be the mechanism of nucleating the connections between myofibrils and focal adhesions (i.e., DSFs). The concept of centripetal assembly was first proposed in 1984 in nonmuscle cells, where stress fibers arise at the edge and elongate in a centripetal manner toward the middle of the cell (Wang, 1984). Subsequent studies established this mode of assembly to be driving DSF formation, but not the assembly of actin arcs (Hotulainen and Lappalainen, 2006). This concept of centripetal assembly was applied to myofibril formation as early as 1990, where vinculin "plaques" at the edge were proposed to give rise to the precursors of myofibrils (Lu *et al.*, 1992). Our data argue while myofibrils do not directly arise from adhesions through centripetal assembly, DSFs that link myofibrils to adhesions are likely to arise due to centripetal assembly. In support of this idea, disruption of β1 integrin in skeletal muscle in vitro led to the absence of mature myofibrils, but not MSF-like structures (Schwander *et al.*, 2003).

Cell–cell adhesion is another source of balancing forces generated by myofibrils (Liu *et al.*, 2016). However, cell–cell adhesion is still unknown to play a significant role in de novo myofibril assembly. It has been demonstrated previously that cell–ECM adhesion sites are responsible for the majority of traction force generation during early cardiomyocyte spreading; as the cell continues to spread and makes cell–cell contacts, load-bearing sites are transferred to cell–cell contact sites (McCain *et al.*, 2012). As such, it is interesting to note that focal adhesion proteins such as FAK and vinculin also localize to intercalated discs once they form (Koteliansky and Gneushev, 1983; Yi *et al.*, 2003). Indeed, a recent study found that vinculin localizes to cell–cell-adhesion sites under increased load in zebrafish hearts in vivo, driving the thickening of myofibrils (Fukuda *et al.*, 2019). Determining the mechanisms driving the localization of such proteins to sites of increased load should be the focus of future studies.

Finally, we show a similar actin architecture in spreading hiCMs, namely, a force-generating contractile stress fiber (i.e., MSFs and myofibrils) connected to a load-bearing structure (i.e., focal adhesion) via a noncontractile stress fiber (i.e., DSF) that is commonly observed in mesenchymal cells. It is interesting to note while this architecture is conserved, there are minor differences in the regulatory mechanisms between the formation of MSFs and actin arcs (Fenix *et al.*, 2018). We speculate that this may allow a mesodermal progenitor cell to modify the same mechanical system to perform two distinct functions, cell migration in the case of mesenchymal lineages and sarcomere assembly in the case of cardiac lineages.

MATERIALS AND METHODS

Material availability

Further information and requests for resources and reagents should be directed to and will be fulfilled by the corresponding author, Dylan Burnette. Key reagents and resources are summarized in Table 1.

Cell culture

Human iPSC-derived cardiomyocytes (CMM-100-012-000.5, Cellular Dynamics, Madison, WI) were cultured as per manufacturer's instructions in proprietary manufacturer-provided cardiomyocyte maintenance medium in polystyrene 96-well cell culture plates.

Cells were maintained at 37°C and 5% CO_2. For replating hiCMs onto glass substrates, cells were washed 2× with 100 µl 1× phosphate-buffered saline (PBS) with no Ca^{2+}/Mg^{2+} (PBS*, 70011044, Life Technologies, Grand Island, NY). PBS* was completely removed from hiCMs, and 40 µl 0.1% Trypsin-EDTA with no phenol red (15400054, Life Technologies, Grand Island, NY) was added to hiCMs and incubated at 37°C for 2 min. Following incubation, the cells were washed 3× with trypsin, the plate was rotated 180 degrees, and the cells were washed another 3×. Trypsinization was then quenched by adding 160 µl of culture media and total cell mixture was pipetted into a 1.5-ml Eppendorf tube. Cells were centrifuged at 200 × *g* for 5 min, and the supernatant was aspirated.

Reagent or resource	Source	Identifier
Antibodies		
Mouse monoclonal anti-alpha actinin 2 (Clone EA-53)	Sigma	A7811
Mouse monoclonal anti-paxillin	BD Biosciences	610051
Rabbit polyclonal anti- DIAPH1	Bethyl Laboratories	A300-078A
Mouse monoclonal anti-FAK	BD Biosciences	610088
Rabbit monoclonal anti-pFAK Y397	Abcam	Ab81298
Mouse monoclonal anti-Titin (9 D10)	DHSB	9D10
Goat anti-mouse 488	Life Technologies	A11001
Goat anti-rabbit 488	Life Technologies	A11034
Goat anti-mouse 568	Life Technologies	A11004
Goat anti-rabbit 568	Life Technologies	A11036
Bacterial and virus strains		
Biological samples		
BSA	RPI	A30075-100.0
Chemicals, peptides, and recombinant proteins		
Phalloidin Alexa Fluor 488	Life Technologies	A12379
Phalloidin Alexa Fluor 568	Life Technologies	A12380
FAK inhibitor PF-573228	Sigma	PZ0117
PBS, 10×, Ca^{2+}/Mg^{2+} free	Life Technologies	70011-044
PFA, 16%	Electron Microscopy Sciences	15710
PBS, 10×, with Ca^{2+}/Mg^{2+}	Corning	46-013-CM
0.5% Trypsin	Life Technologies	15400-054
0.1% Gelatin	Sigma	ES-006-B
Dimethyl sulfoxide	Sigma	276855
Vectashield with DAPI	Vector	H-1200
Triton X-100	Fisher Scientific	BP151100
Critical commercial assays		
Mix-N-Stain Antibody Labeling kit	Biotium	92233
Deposited data		
Experimental models: cell lines		
iCell cardiomyocytes^2 kit	Cell Dynamics International	CMC-100-012-000.5
Experimental models: organisms/strains		
Oligonucleotides		
SMART Pool siRNA against human FAK5′-AAACGUCGAAAAUUGAUUG-3′,5′-AAACGUCGAAAAUUGAUUG-3′, 5′-CAGCAUUUCGUCAU-AAGGC-3′, 5′-AGACAACCCAACUUCAAAG-3′	Horizon Discovery	E-003164-00-0005
SMART Pool siRNA against human DIAPH15′-CUGUCUUUGAAUC-CAACAC-3′, 5′-CACUAAUAAUAAAUAACCA-3′, 5′-UGAUAUUGAAGC-CAAAAGC-3′, 5′-AAGUCAUCCAUCUCCAUGC-3′	Horizon Discovery	E-010347-00-0005
SMART Pool siRNA against human VCL5′-UUCGAAUUUUGAUUG-AAGC-3′, 5′-CAACCUUAAUAAAUGCUGG-3′, 5′-AGUCUAUGGAGGC-CAAUGC-3′, 5′-ACAAAUCCUAGCUUAUAAA-3′	Horizon Discovery	E-009288-00-0005
Recombinant DNA		
mApple-Lifeact	Addgene	54747
mEmerald-Lifeact	Addgene	54148
mCherry-Paxillin	Addgene	55114

TABLE 1: Key resources

Continues

Reagent or resource	Source	Identifier
mCherry-Alpha-actinin-2	Addgene	54974
Talin Head-mEGFP	Addgene	56448
Talin-mEGFP	Addgene	56446
Software and algorithms		
MATLAB code to analyze Z-line length and adhesion area	This study	
Fiji (Fiji Is Just ImageJ)	National Institutes of Health	
Nikon elements	Nikon	
Other		

TABLE 1: Key resources. Continued.

The cell pellet was resuspended in 200 µl of culture media and plated on 35-mm dishes with a 10-mm glass bottom (D35-10-1.5-N; CellVis, Sunnydale, CA) precoated with 10 µg/ml fibronectin (354008, Corning) for 1 h at 37°C.

Chemicals

FAK inhibitor PF-228 (PZ0117) was purchased from Sigma. Alexa Fluor 488-phalloidin (A12379), Alexa Fluor 568-phalloidin (A12380), Alexa Fluor 488-goat anti-mouse (A11029), Alexa Fluor 488-goat anti-rabbit (A11034), Alexa Fluor 568-goat-anti-rabbit (A11011), and Alexa Fluor 568-goat anti-mouse (A11004) antibodies were purchased from Life Technologies (Grand Island, NY).

Mouse anti-Paxillin (1:200, 610051) and mouse anti-FAK (1:500, 610088) antibodies were purchased from BD Biosciences. Rabbit anti-FAK pY357 (1:200, ab81298) was purchased from Abcam. Mouse anti-α-actinin 2 (1:200, A7811) was purchased from Sigma Aldrich. Titin (9D10) antibody was purchased from the Developmental Studies Hybridoma Bank (University of Iowa). Primary antibody conjugation was performed using Mix-n-Stain kits (92233) purchased from Biotium (Fremont, CA) according to the instructions provided by the manufacturer. Paraformaldehyde (PFA, 15710) was purchased from Electron Microscopy Sciences (Hatfield, PA). Triton X-100 (BP151100) was purchased from Fisher Scientific (Suwanee, GA).

Fixation and immunostaining

Cells were fixed with 4% PFA in PBS at room temperature for 20 min and then permeabilized for 5 min with 1% Triton X-100/4% PFA in PBS as previously described (Burnette *et al.*, 2014). For actin visualization, phalloidin 488 or 568 in 1× PBS (15 µl of stock phalloidin per 200 µl of PBS) was used for 2 h at room temperature. For immunofluorescence experiments, cells were blocked in 10% bovine serum albumin (BSA) in PBS for 20 min, followed by antibody incubations.

For visualizing titin, a live-cell extraction was performed to remove cytoplasmic background as described previously (Burnette *et al.*, 2011). Briefly, a cytoskeleton-stabilizing live-cell extraction buffer was made fresh containing 2 ml of stock solution (500 mM 1,4-piperazinediethanesulfonic acid, 25 mM ethylene glycol tetra acetic acid, 25 mM $MgCl_2$), 4 ml of 10% polyoxyethylene glycol (PEG; 35,000 molecular weight), 4 ml H_2O, and 100 µl of Triton X-100, 10 µM paclitaxel, and 10 µM phalloidin. Cells were treated with this extraction buffer for 1 min, followed by a 1-min wash with wash buffer (extraction buffer without PEG or Triton X-100). Cells were then fixed with 4% PFA for 20 min, followed by antibody labeling. VectaShield with DAPI (H-1200, Vector Laboratories, Burlingame, CA) was used for mounting.

Protein expression

For protein expression in hiCMs, 200 ng plasmid and 0.4 µl ViaFect (E4981, Promega, Madison WI) were added to a total of 10 µl of Opti-MEM (ThermoFisher, Waltham, MA) and added to a single well of hiCMs in a 96-well plate. The transfection was incubated overnight (~16 h) prior to plating for imaging.

Plasmids

All plasmids used in this study are available from Addgene (Cambridge, MA). mCherry-Alpha-Actinin2-N-18 (Addgene plasmid #54974), mApple-Lifeact-7 (Addgene plasmid #54747), mEmerald-Lifeact-7 (Addgene plasmid #54148), mCherry-Paxillin-22 (Addgene plasmid #55114) (Paszek *et al.*, 2012), EGFP-Talin-H-18 (Addgene plasmid #56448), and EGFP-Talin-CW-18 (Addgene plasmid # 56446) were gifts from Michael Davidson.

Knockdown experiments

Knockdowns for FAK (PTK2), DIAPH1, and VCL were performed using Accell SmartPool siRNA (PTK2: E-003164-00-0005; DIAPH1: E-010347-00-0005; VCL: E-009288-00-0005; scrambled control: D-001910-10-05) purchased from GE Dharmacon. Experiments were performed in 96-well culture plates using the TransIT-TKO transfection reagent using instructions provided by the manufacturer (MIR2154, Mirus Bio). Single siRNA-mediated knockdown experiments were performed using PTK2: A-003164-21-0005; DIAPH1: A-010347-14-0005; VCL: A-009288-13-0005; and scrambled control: D-001910-10-05 were purchased from GE Dharmacon. Three consecutive rounds of knockdown were performed to deplete protein levels. Following knockdown, cells were replated onto glass substrates for 24 h and fixed for immunofluorescence or lysed for Western blotting.

Western blotting

Gel samples were prepared by mixing cell lysates with LDS sample buffer (Life Technologies, NP0007) and sample reducing buffer (Life Technologies, NP0009) and boiled at 95°C for 5 min. Samples were resolved on Bolt 4–12% gradient Bis-Tris gels (Life Technologies, NW04120BOX). Protein bands were blotted onto a nylon membrane (Millipore). Blots were blocked using 5% nonfat dry milk (Research Products International, Mt. Prospect, IL, M17200) in Tris-buffered saline Tween-20 (TBST). Antibody incubations were also performed in 5% NFDM in TBST. Blots were developed using the Immobilon Chemiluminescence Kit (Millipore, WBKLS0500).

SIM

SIM imaging and processing was performed using a GE Healthcare DeltaVision OMX equipped with a 60 × 1.42 NA Oil objective and

sCMOS camera or using a Nikon N-SIM equipped with a 100 × 1.49 NA Oil objective and EMCCD camera.

Fluorescence, live-cell microscopy, and focused laser-mediated cutting

High-resolution widefield fluorescence images (for Z-line measurement) and live imaging of actin filaments (to measure MSF translocation rates) were acquired on a Nikon Eclipse Ti equipped with a Nikon 100× Plan Apo 1.45 numerical aperture (NA) oil objective and a Nikon DS-Qi2 CMOS camera. Live imaging for Figure 2 and focused laser-mediated cutting for Figure 1 were performed on a Nikon Spinning Disk confocal microscope equipped with a 60 × 1.4 NA objective and an Andor iXON Ultra EMCCD camera, provided by the Nikon Center of Excellence, Vanderbilt University. Cutting of DSFs was performed using a 100 mW UV laser (Coherent Technologies) at 75% power, using a dwell time of 500 µs for a total period of 1 s. TIRF imaging was performed using a Nikon TiE inverted light microscope equipped with a 100 × 1.49 NA TIRF objective and an Andor Neo sCMOS camera. Cells were maintained at 37°C with 5% CO_2 using a Tokai Hit stage incubator.

Quantification and statistical analysis

To measure Z-line length in hiCMs, Z-sections were acquired at 200-nm intervals using widefield imaging at 100 × with 1.5 Zoom. Images were deconvolved with the Automatic deconvolution using Nikon Elements software. All α-actinin 2 structures were 3D thresholded manually in Nikon Elements using the clean algorithm 3×. The lengths of the major axis of each body were exported from Elements for the calculation of Z-line length. Using a length minimum exclusion criterion of 0.2 µm, Z-line lengths were calculated using MATLAB (supplementary software).

To measure sum adhesion area of hiCMs, one single Z-slice of a reconstructed SIM image where the focal adhesions were in focus was selected. Focal adhesions were thresholded and the sum area was measured in Fiji using a size minimum exclusion criterion of 0.1 μm^2.

For measurement of the distance of titin to the edge (Figure 3, F and G), we measured the length of a line from the edge to the first titin ring in Fiji. The researcher analyzing the data was blinded to treatment groups.

For measurement of MSF translocation rates, hiCMs were transfected with Lifeact-mApple and allowed to spread for 16 h post-plating. Two Z-sections were acquired, one at the ventral plane and one 0.5 µm above the ventral plane, at 2-min intervals for a total time of 2 h. Maximum Z-projections were performed on the time montages, followed by alignment of the image stacks using the StackReg plugin in Fiji. A 3 pixel-thick line was drawn parallel to the direction of MSF translocation to create a kymograph, following which the rates were measured for MSFs; 1–3 trajectories were counted for each cell.

Statistical significance was determined using unpaired two-tailed Student's *t* tests performed in MATLAB or Excel. Each experiment was performed a minimum of 3× and each cell was counted as a data point and pooled over the biological replicates. All data were displayed as Tukey plots, which were represented with boxes (with Q1, median, Q3 percentiles), whiskers (minimum and maximum values within 1.5 times interquartile range), and outliers (solid circles). No outliers were removed from the analysis. For Western blot graphs, error bars represent standard error of the means.

ACKNOWLEDGMENTS

We thank the Nikon Center of Excellence, Vanderbilt University, for providing access to the Nikon spinning-disk microscope and technical support. We thank Matthew Tyska for providing access to his TIRF microscope. The raw data generated in the current study are available from the corresponding author on reasonable request. This work was funded by a Maximizing Investigators' Research Award from the National Institute of General Medical Sciences (R35 GM125028) awarded to D.T.B., an American Heart Association Predoctoral Fellowship (18PRE33960551) to N.T., and Vanderbilt University School of Medicine Program in Developmental Biology training grant T32-HD007502 to A.C.N.

REFERENCES

Alexandrova AY, Arnold K, Schaub S, Vasiliev JM, Meister JJ, Bershadsky AD, Verkhovsky AB (2008). Comparative dynamics of retrograde actin flow and focal adhesions: formation of nascent adhesions triggers transition from fast to slow flow. PLoS One 3, e3234.

Bloor JW, Brown NH (1998). Genetic analysis of the Drosophila alphaPS2 integrin subunit reveals discrete adhesive, morphogenetic and sarcomeric functions. Genetics 148, 1127–1142.

Burnette DT, Manley S, Sengupta P, Sougrat R, Davidson MW, Kachar B, Lippincott-Schwartz J (2011). A role for actin arcs in the leading-edge advance of migrating cells. Nat Cell Biol 13, 371–381.

Burnette DT, Shao L, Ott C, Pasapera AM, Fischer RS, Baird MA, Der Loughian C, Delanoe-Ayari H, Paszek MJ, Davidson MW, *et al.* (2014). A contractile and counterbalancing adhesion system controls the 3D shape of crawling cells. J Cell Biol 205, 83–96.

Carisey A, Ballestrem C (2011). Vinculin, an adapter protein in control of cell adhesion signalling. Eur J Cell Biol 90, 157–163.

Case LB, Baird MA, Shtengel G, Campbell SL, Hess HF, Davidson MW, Waterman CM (2015). Molecular mechanism of vinculin activation and nanoscale spatial organization in focal adhesions. Nat Cell Biol 17, 880–892.

Chopra A, Kutys ML, Zhang K, Polacheck WJ, Sheng CC, Luu RJ, Eyckmans J, Hinson JT, Seidman JG, Seidman CE, *et al.* (2018). Force generation via beta-cardiac myosin, titin, and alpha-actinin drives cardiac sarcomere assembly from cell-matrix adhesions. Dev Cell 44, 87–96.e85.

Dabiri BE, Lee H, Parker KK (2012). A potential role for integrin signaling in mechanoelectrical feedback. Prog Biophys Mol Biol 110, 196–203.

Dabiri GA, Turnacioglu KK, Sanger JM, Sanger JW (1997). Myofibrillogenesis visualized in living embryonic cardiomyocytes. Proc Natl Acad Sci USA 94, 9493–9498.

del Rio A, Perez-Jimenez R, Liu R, Roca-Cusachs P, Fernandez JM, Sheetz MP (2009). Stretching single talin rod molecules activates vinculin binding. Science 323, 638–641.

Dlugosz AA, Antin PB, Nachmias VT, Holtzer H (1984). The relationship between stress fiber-like structures and nascent myofibrils in cultured cardiac myocytes. J Cell Biol 99, 2268–2278.

Dumbauld DW, Lee TT, Singh A, Scrimgeour J, Gersbach CA, Zamir EA, Fu J, Chen CS, Curtis JE, Craig SW, *et al.* (2013). How vinculin regulates force transmission. Proc Natl Acad Sci USA 110, 9788–9793.

Fenix AM, Neininger AC, Taneja N, Hyde K, Visetsouk MR, Garde RJ, Liu B, Nixon BR, Manalo AE, Becker JR, *et al.* (2018). Muscle-specific stress fibers give rise to sarcomeres in cardiomyocytes. Elife 7.

Fessenden TB, Beckham Y, Perez-Neut M, Ramirez-San Juan G, Chourasia AH, Macleod KF, Oakes PW, Gardel ML (2018). Dia1-dependent adhesions are required by epithelial tissues to initiate invasion. J Cell Biol 217, 1485–1502.

Fukuda R, Gunawan F, Ramadass R, Beisaw A, Konzer A, Mullapudi ST, Gentile A, Maischein HM, Graumann J, Stainier DYR (2019). Mechanical Forces Regulate Cardiomyocyte Myofilament Maturation via the VCL-SSH1-CFL Axis. Dev Cell 51, 62–77.e65.

Geiger B, Spatz JP, Bershadsky AD (2009). Environmental sensing through focal adhesions. Nat Rev Mol Cell Biol 10, 21–33.

Gupton SL, Waterman-Storer CM (2006). Spatiotemporal feedback between actomyosin and focal-adhesion systems optimizes rapid cell migration. Cell 125, 1361–1374.

Hersch N, Wolters B, Dreissen G, Springer R, Kirchgessner N, Merkel R, Hoffmann B (2013). The constant beat: cardiomyocytes adapt their forces by equal contraction upon environmental stiffening. Biol Open 2, 351–361.

Hotulainen P, Lappalainen P (2006). Stress fibers are generated by two distinct actin assembly mechanisms in motile cells. J Cell Biol 173, 383–394.

Hresko MC, Williams BD, Waterston RH (1994). Assembly of body wall muscle and muscle cell attachment structures in Caenorhabditis elegans. J Cell Biol 124, 491–506.
Jacot JG, McCulloch AD, Omens JH (2008). Substrate stiffness affects the functional maturation of neonatal rat ventricular myocytes. Biophys J 95, 3479–3487.
Janostiak R, Pataki AC, Brabek J, Rosel D (2014). Mechanosensors in integrin signaling: the emerging role of p130Cas. Eur J Cell Biol 93, 445–454.
Jiang Y, Park P, Hong SM, Ban K (2018). Maturation of cardiomyocytes derived from human pluripotent stem cells: current strategies and limitations. Mol Cells 41, 613–621.
Kanchanawong P, Shtengel G, Pasapera AM, Ramko EB, Davidson MW, Hess HF, Waterman CM (2010). Nanoscale architecture of integrin-based cell adhesions. Nature 468, 580–584.
Katsumi A, Naoe T, Matsushita T, Kaibuchi K, Schwartz MA (2005). Integrin activation and matrix binding mediate cellular responses to mechanical stretch. J Biol Chem 280, 16546–16549.
Knoll R, Buyandelger B, Lab M (2011). The sarcomeric Z-disc and Z-discopathies. J Biomed Biotechnol 2011, 569628.
Koteliansky VE, Gneushev GN (1983). Vinculin localization in cardiac muscle. FEBS Lett 159, 158–160.
Kovacic-Milivojevic B, Roediger F, Almeida EA, Damsky CH, Gardner DG, Ilic D (2001). Focal adhesion kinase and p130Cas mediate both sarcomeric organization and activation of genes associated with cardiac myocyte hypertrophy. Mol Biol Cell 12, 2290–2307.
Lemke SB, Schnorrer F (2017). Mechanical forces during muscle development. Mech Dev 144, 92–101.
Lemke SB, Weidemann T, Cost AL, Grashoff C, Schnorrer F (2019). A small proportion of Talin molecules transmit forces at developing muscle attachments in vivo. PLoS Biol 17, e3000057.
Liu H, Qin W, Wang Z, Shao Y, Wang J, Borg TK, Gao BZ, Xu M (2016). Disassembly of myofibrils and potential imbalanced forces on Z-discs in cultured adult cardiomyocytes. Cytoskeleton (Hoboken) 73, 246–257.
Loison O, Weitkunat M, Kaya-Copur A, Nascimento Alves C, Matzat T, Spletter ML, Luschnig S, Brasselet S, Lenne PF, Schnorrer F (2018). Polarization-resolved microscopy reveals a muscle myosin motor-independent mechanism of molecular actin ordering during sarcomere maturation. PLoS Biol 16, e2004718.
Lu MH, DiLullo C, Schultheiss T, Holtzer S, Murray JM, Choi J, Fischman DA, Holtzer H (1992). The vinculin/sarcomeric-alpha-actinin/alpha-actin nexus in cultured cardiac myocytes. J Cell Biol 117, 1007–1022.
McCain ML, Lee H, Aratyn-Schaus Y, Kleber AG, Parker KK (2012). Cooperative coupling of cell-matrix and cell-cell adhesions in cardiac muscle. Proc Natl Acad Sci USA 109, 9881–9886.
O'Brien S, Golubovskaya VM, Conroy J, Liu S, Wang D, Liu B, Cance WG (2014). FAK inhibition with small molecule inhibitor Y15 decreases viability, clonogenicity, and cell attachment in thyroid cancer cell lines and synergizes with targeted therapeutics. Oncotarget 5, 7945–7959.
Parsons JT, Martin KH, Slack JK, Taylor JM, Weed SA (2000). Focal adhesion kinase: a regulator of focal adhesion dynamics and cell movement. Oncogene 19, 5606–5613.
Pasapera AM, Schneider IC, Rericha E, Schlaepfer DD, Waterman CM (2010). Myosin II activity regulates vinculin recruitment to focal adhesions through FAK-mediated paxillin phosphorylation. J Cell Biol 188, 877–890.
Paszek MJ, DuFort CC, Rubashkin MG, Davidson MW, Thorn KS, Liphardt JT, Weaver VM (2012). Scanning angle interference microscopy reveals cell dynamics at the nanoscale. Nat Methods 9, 825–827.
Quach NL, Rando TA (2006). Focal adhesion kinase is essential for costamerogenesis in cultured skeletal muscle cells. Dev Biol 293, 38–52.
Rhee D, Sanger JM, Sanger JW (1994). The premyofibril: evidence for its role in myofibrillogenesis. Cell Motil Cytoskeleton 28, 1–24.
Riveline D, Zamir E, Balaban NQ, Schwarz US, Ishizaki T, Narumiya S, Kam Z, Geiger B, Bershadsky AD (2001). Focal contacts as mechanosensors: externally applied local mechanical force induces growth of focal contacts by an mDia1-dependent and ROCK-independent mechanism. J Cell Biol 153, 1175–1186.
Samarel AM (2005). Costameres, focal adhesions, and cardiomyocyte mechanotransduction. Am J Physiol Heart Circ Physiol 289, H2291–H2301.
Sanger JW, Kang S, Siebrands CC, Freeman N, Du A, Wang J, Stout AL, Sanger JM (2005). How to build a myofibril. J Muscle Res Cell Motil 26, 343–354.
Schaller MD, Hildebrand JD, Shannon JD, Fox JW, Vines RR, Parsons JT (1994). Autophosphorylation of the focal adhesion kinase, pp125FAK, directs SH2-dependent binding of pp60src. Mol Cell Biol 14, 1680–1688.
Schwander M, Leu M, Stumm M, Dorchies OM, Ruegg UT, Schittny J, Muller U (2003). Beta1 integrins regulate myoblast fusion and sarcomere assembly. Dev Cell 4, 673–685.
Sharp WW, Simpson DG, Borg TK, Samarel AM, Terracio L (1997). Mechanical forces regulate focal adhesion and costamere assembly in cardiac myocytes. Am J Physiol 273, H546–H556.
Simpson DG, Decker ML, Clark WA, Decker RS (1993). Contractile activity and cell-cell contact regulate myofibrillar organization in cultured cardiac myocytes. J Cell Biol 123, 323–336.
Slack-Davis JK, Martin KH, Tilghman RW, Iwanicki M, Ung EJ, Autry C, Luzzio MJ, Cooper B, Kath JC, Roberts WG, *et al*. (2007). Cellular characterization of a novel focal adhesion kinase inhibitor. J Biol Chem 282, 14845–14852.
Sparrow JC, Schock F (2009). The initial steps of myofibril assembly: integrins pave the way. Nat Rev Mol Cell Biol 10, 293–298.
Swaminathan V, Kalappurakkal JM, Mehta SB, Nordenfelt P, Moore TI, Koga N, Baker DA, Oldenbourg R, Tani T, Mayor S, *et al*. (2017). Actin retrograde flow actively aligns and orients ligand-engaged integrins in focal adhesions. Proc Natl Acad Sci USA 114, 10648–10653.
Tan CL, Kwok JC, Heller JP, Zhao R, Eva R, Fawcett JW (2015). Full length talin stimulates integrin activation and axon regeneration. Mol Cell Neurosci 68, 1–8.
Taneja N, Fenix AM, Rathbun L, Millis BA, Tyska MJ, Hehnly H, Burnette DT (2016). Focal adhesions control cleavage furrow shape and spindle tilt during mitosis. Sci Rep 6, 29846.
Thievessen I, Thompson PM, Berlemont S, Plevock KM, Plotnikov SV, Zemljic-Harpf A, Ross RS, Davidson MW, Danuser G, Campbell SL, *et al*. (2013). Vinculin-actin interaction couples actin retrograde flow to focal adhesions, but is dispensable for focal adhesion growth. J Cell Biol 202, 163–177.
Tojkander S, Gateva G, Husain A, Krishnan R, Lappalainen P (2015). Generation of contractile actomyosin bundles depends on mechanosensitive actin filament assembly and disassembly. Elife 4, e06126.
Volk T, Fessler LI, Fessler JH (1990). A role for integrin in the formation of sarcomeric cytoarchitecture. Cell 63, 525–536.
Wang SM, Greaser ML (1985). Immunocytochemical studies using a monoclonal antibody to bovine cardiac titin on intact and extracted myofibrils. J Muscle Res Cell Motil 6, 293–312.
Wang YL (1984). Reorganization of actin filament bundles in living fibroblasts. J Cell Biol 99, 1478–1485.
Yang KC, Breitbart A, De Lange WJ, Hofsteen P, Futakuchi-Tsuchida A, Xu J, Schopf C, Razumova MV, Jiao A, Boucek R, *et al*. (2018). Novel Adult-onset systolic cardiomyopathy due to MYH7 E848G mutation in patient-derived induced pluripotent stem cells. JACC Basic Transl Sci 3, 728–740.
Yi XP, Wang X, Gerdes AM, Li F (2003). Subcellular redistribution of focal adhesion kinase and its related nonkinase in hypertrophic myocardium. Hypertension 41, 1317–1323.
Yuan H, Marzban B, Kit Parker K (2017). Myofibrils in cardiomyocytes tend to assemble along the maximal principle stress directions. J Biomech Eng 139.